THE PHYSICAL NATURE OF THE LOOP-TOP X-RAY SOURCES IN THE GRADUAL PHASE OF SOLAR FLARES

NARIAKI V. NITTA

Lockheed Martin Solar and Astrophysics Laboratory, O/L9-41, B/252, 3251 Hanover Street, Palo Alto, CA 94304; nitta@lmsal.com

JUN SATO

NASA Goddard Space Flight Center, Code 681, Greenbelt, MD 20771

AND

HUGH S. HUDSON

Solar Physics Research Corporation/Institute of Space and Astronautical Science, 3-1-1 Yoshinodai, Sagamihara, Kanagawa 229, Japan

ABSTRACT

We have analyzed *Yohkoh* soft and hard X-ray images of 36 flares, primarily to study the loop-top source that often prevails in these wavelengths during and following the impulsive phase. There are typically two patterns for the location of the low-energy (15–30 keV) hard X-ray (HXR) source with respect to the soft X-ray (SXR) loop. In a quarter of the flares, the HXR source lies in an extended structure separate from the brightest SXR loop. In other flares, the HXR source appears to be part of the same bipolar structure as the SXR loop, but its centroid is often displaced from the SXR loop-top source. The fact that the HXR source is not cospatial with the SXR source may reflect the presence of a distinct hotter structure. According to *Yohkoh* X-ray emission-line spectroscopy, the ~ 20 MK plasma accounts for only a fraction of the HXR counts. The temperature maps obtained from the SXR broadband photometry occasionally reveal high-temperature areas outside the bright loop, but they also tend to be displaced from the HXR source, indicating that they do not represent the superhot ($\gtrsim 30$ MK) plasma. We discuss possible distributions of plasma of different temperatures that could be consistent with the data.

Subject headings: plasmas — Sun: flares — Sun: X-rays, gamma rays

1. INTRODUCTION

A striking feature of many solar flares observed with the Soft X-ray Telescope (SXT; Tsuneta et al. 1991) on board *Yohkoh* (Ogawara et al. 1991) is the presence of a compact soft X-ray (SXR) source at what seems to be a loop top (Acton et al. 1992; Feldman et al. 1994; Doschek, Strong, & Tsuneta 1995), sometimes preceded by a short interval at which loop footpoint sources are seen even in soft X-rays (Hudson et al. 1994). The temperature of this loop-top source is typically $\lesssim 15$ MK, as calculated from the ratio of SXT images in the two thickest filters (McTiernan et al. 1993; Doschek 1999). The broadband nature of the SXT temperature response means that a temperature map from a single filter ratio may not properly reveal the presence of a hotter component (Nitta & Yaji 1997). Such additional hot material might explain, for example, the temperature of $\gtrsim 20$ MK as obtained in (spatially unresolved) diagnostics on Fe xxv and xxvi lines, as compared with ~ 15 MK from Ca xix lines (see, e.g., Doschek & Feldman 1987).

In fact, Jakimiec et al. (1998) proposed a turbulent magnetic field model to explain the coexistence of both cool (~ 10 MK) and hot (~ 20 MK) plasma at the loop top. This was based partly on their finding that the low-energy hard X-ray (HXR) source in the images from the *Yohkoh* Hard X-ray Telescope (HXT; Kosugi et al. 1991) typically coincides with the SXR loop-top source. However, their 36 flares contain at least one exception, where the dominant HXR flux comes from an extended structure away from the bright SXR loop (Nitta & Yaji 1997). Moreover, Jakimiec et al. (1998) did not discuss the possible contributions of

superhot[1] plasma in the HXT data, even though they analyzed a subset of the Fe xxvi flares compiled by Pike et al. (1996). According to Pike et al. (1996), at least four of the flares of Jakimiec et al. (1998) have T(Fe xxvi) $\gtrsim 30$ MK. In addition, the ratio of the two lowest-energy channels of HXT also indicates temperatures much higher than 20 MK (Hudson & Nitta 1996) for most of the flares analyzed by Pike et al. (1996).

Despite its potential importance in understanding the flare mechanisms, because it shows the most intense heating, the existence of superhot plasma has not been confirmed as compellingly as it was when first unveiled with high-resolution HXR spectroscopy (Lin et al. 1981) and diagnostics on Fe xxvi lines (Tanaka 1986). This is largely because of the lack of continuum spectra with comparable resolution. In recent years, however, the temperatures from the HXT channel ratio have been routinely used as an indicator of the superhot component, sometimes in connection with an attempt to distinguish different types of magnetic field geometry involved in magnetic reconnection (see, e.g., Sakao, Kosugi, & Masuda 1998).

In this paper, we try to understand the distribution of plasma with different temperatures, including those in the superhot range, by comparing SXT and HXT images in detail for the 36 flares analyzed by Jakimiec et al. (1998). In particular, we clarify the relationship between the loop-top source, as observed in the HXT low-energy channels during

---

[1] Here, "superhot" refers to any independent hotter component, but specifically to sources at $\gtrsim 30$ MK as originally found by Lin et al. (1981).

the gradual phase (see, e.g., Masuda 1994), and the SXT high-temperature pixels that occasionally appear outside the loop (see, e.g., Doschek 1999); the Appendix reviews the systematic errors in SXT temperature maps on the basis of our current knowledge. In § 2, we make an overview of the study, showing variations of the appearance of the flares and, more specifically, in the pattern of the location of the low-energy HXR source with respect to the SXR loop-top source, observations not presented in the Jakimiec et al. (1998) study. Section 3 presents and discusses in more detail the results for all the flares. In showing the observational results, we implicitly bear in mind qualitative predictions from the simple reconnection models, such as the presence of superhot regions outside the flare loop and the rising motion of the loop-top source. We describe in § 4 a possible distribution of the multitemperature plasma that is consistent with data.

2. ANALYSIS

We compare registered SXT images in three filters (thin Al, thick Al, and Be) with synthesized HXT images in three channels, L (14–23 keV), M1 (23–33 keV), and M2 (33–53 keV). The availability of HXT images depends largely on count rates. The accuracy of the co-alignment between SXT and HXT images is estimated to be $\lesssim 1''$ (Masuda 1994), or better than half of the SXT full-resolution pixel, which is $2''.46$. We also make SXT temperature maps on the basis of the ratio of images in the thickest filters, Be and thick Al.

For this study, we adopt two improvements recently incorporated into the standard *Yohkoh* data analysis software. One concerns HXT and the other SXT. First, we adopt an improved set of modulation patterns for HXT and a new algorithm to estimate the total flux, increasing the reliability of image reconstruction (Sato, Kosugi, & Makishima 1999). Second, we use an orbit-dependent dark subtraction, as implemented by T. Metcalf and S. Freeland, which may be important in analyzing faint pixels in SXT images. Note that the SXT high-temperature regions are often seen in these areas.

Our analysis is illustrated by two figures for one of the 36 flares. Figure 1 shows its X-ray light curves and three representative intervals, A, B, and C, as indicated by pairs of dotted or dashed lines. These are taken from the intervals used for HXT image reconstruction. Interval A represents the impulsive phase, usually characterized by sharp spikes with harder spectra than at other times. This interval is used to look for double-footpoint sources. When we do not see them in interval A, we also look at images from slightly before and after. HXT light curves at later times are characterized by more gradual variations with softer spectra. Interval B corresponds to the first interval after interval A at which the HXT image in the L channel shows a single source, presumably located at the loop top. We make various comparisons at this interval. Interval C is added so that we see how the X-ray sources change while the light curves are undergoing a featureless decay.

The images of this flare, as given in the top and middle panels of Figure 2, seem to conform to the usual scenario of chromospheric evaporation for a loop flare. In interval A, a clear double-source structure is seen in hard X-rays (even in the L channel), presumably representing bombardment of nonthermal electrons into the footpoints of a coronal loop system, which would initially have low gas pressure. Then the loop becomes brighter, consistent with filling by evapo-
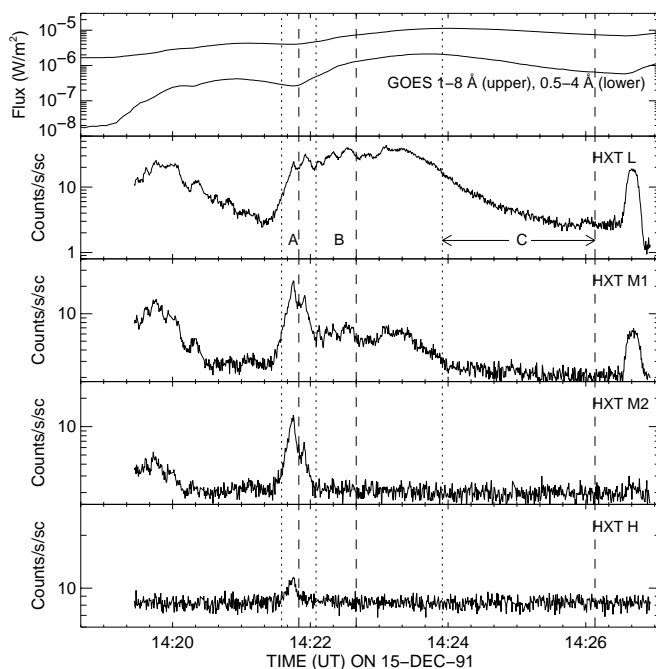

FIG. 1.—Light curves of the 1991 December 15 flare (event 1). From top to bottom: *GOES* (1–8 Å and 0.5–4 Å), HXT L (14–23 keV), M1 (23–33 keV), M2 (33–53 keV), and H (53–93 keV) channels. Pairs of dotted and dashed lines indicate the three intervals for which synthesized HXT images are compared in Fig. 2 with SXT intensity and temperature images.
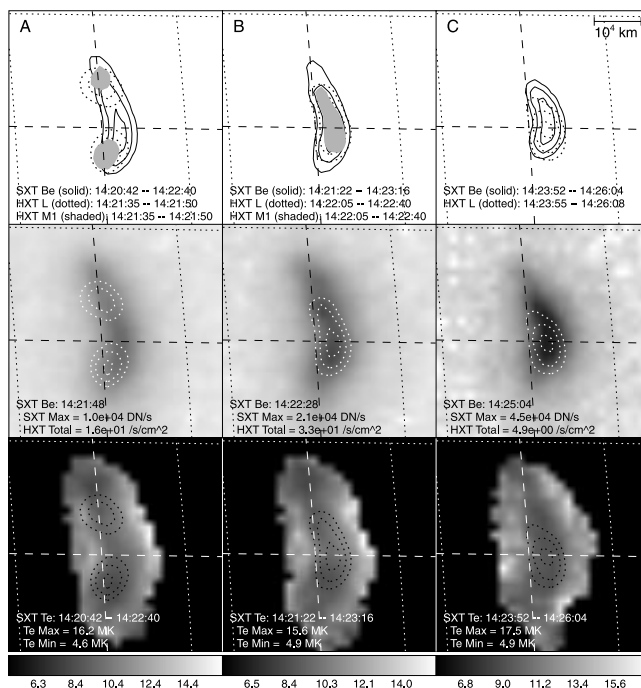

FIG. 2.—X-ray images of the 1991 December 15 flare (event 1). See Fig. 1 for the three integration periods (*A, B, and C*) used for the hard X-ray images presented. HXT L-channel images appear in dotted contours co-aligned with the following images: *top*, HXT M1-channel images (shaded areas have more than 30% of the peak intensity) and SXT images in Be filter summed for matching intervals (*solid contours*); *middle*, SXT snapshots in Be filter taken close in time to the centers of the intervals (*gray scale*); *bottom*, SXT temperature maps obtained from the ratio of images in Be and thick Al filters, summed for matching intervals. Contour levels are 30%, 50%, and 80% of the peaks of the individual images. Latitudinal and longitudinal grids are given at 2° separation. Dashed lines indicate N06 and W41.
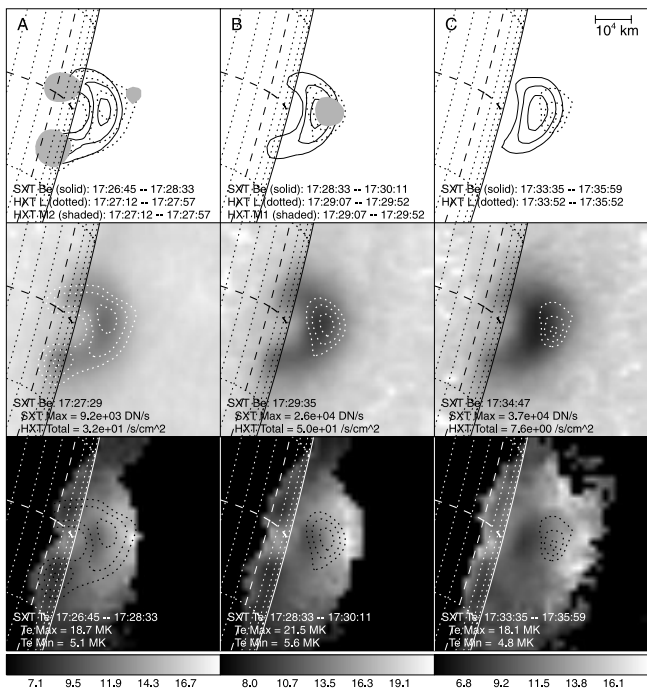
FIG. 3.—X-ray images of the 1992 January 13 flare (event 6). Same format as Fig. 2, except that an HXT M2-channel image is shown in *A* down to 15% of the peak (to emphasize the above-the-loop-top source identified by Masuda et al. 1994). Dashed lines indicate S15 and W83.

FIG. 5.—Images of the 1992 July 3 flare in a larger field-of-view: (*a*) SXT half-resolution image, (*b*) continuum image around 6302 Å, (*c*) line-of-sight magnetogram, and (*d*) Hα + 350 mÅ image. Images (*b*)–(*d*) were taken with the Swedish Vacuum Telescope at La Palma. Boxes indicate the field of view of Fig. 4. Dashed lines indicate N12 and E26.

rated plasma. In this particular flare, the offset between the loop-top source as seen in the SXT Be filter image and the HXT L-channel image is almost negligible.

Examining the whole data set, we have learned that this flare is rather exceptional. First, the loop-top source seen in
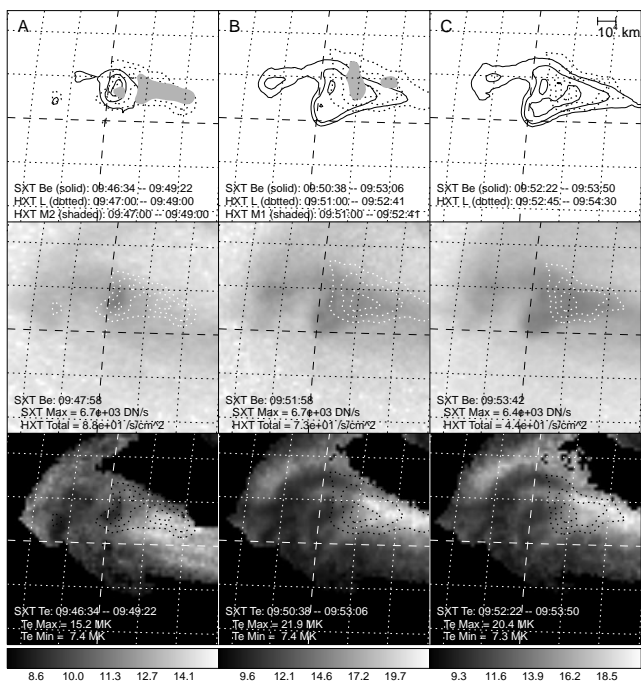

FIG. 4.—X-ray images of the 1992 July 3 flare (event 17). Same format as Fig. 2, except that an HXT M2-channel image is shown in *A*. Dashed lines indicate N12 and E28.
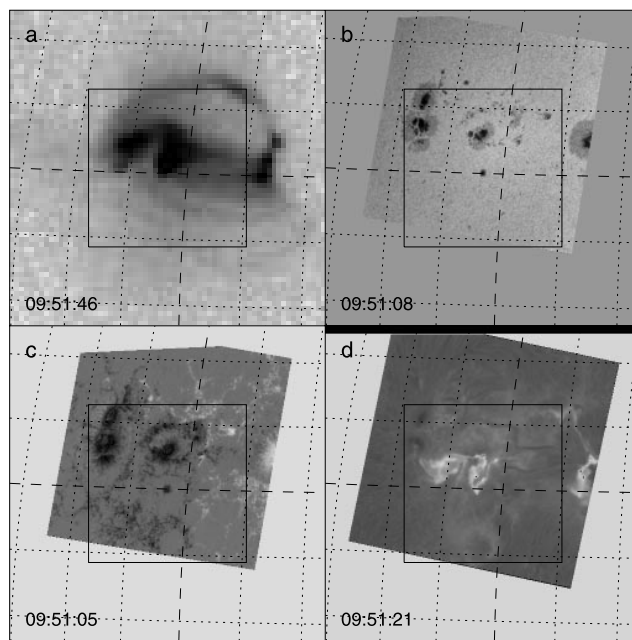
the HXT L channel is usually not cospatial with that seen in the SXT Be filter; as shown below, 26 of the 36 events have offsets exceeding 1 SXT pixel (2″.46), a conservative value for the accuracy of the SXT-HXT co-alignment. Note that the Masuda (1994) co-alignment of SXT and HXT, based on similar comparisons, achieved higher accuracy, presumably because of a statistical approach with carefully selected events. For limb flares, the centroid of the loop-top source in the HXT L channel is often located higher than that in SXT Be filter. The term "higher" here means that the HXT source is located radially farther away from disk center, as would be expected if the sources lay in the same plane. Such an example is shown in Figure 3 (intervals B and C). This is the famous "Masuda" flare, which occurred on 1992 January 13 (see, e.g., Masuda et al. 1994). Except for the above-the-loop-top source in the HXT M2 channel (interval A), it otherwise appears as an ordinary loop flare, in the sense that the two footpoints in the impulsive phase evolve into loop-top emission in the gradual phase. As a more striking example, Figure 4 gives images of another flare (on disk), in which the hard X-rays come from an extended structure separate from the soft X-rays. It is hard to identify footpoints or otherwise identify loops in the HXR images, although the larger-scale SXT views in Figure 5 clearly reveal their presence.

3. CHARACTERISTICS OF FLARES

3.1. *Light Curves*

Here we review the spatially unresolved characteristics of the 36 flares studied, which are summarized in Table 1. The first three columns show the event number, date, and time of the HXR peak. A few flares missed the HXR peak. The fourth column is the reference time, which is the center of interval B, shortly after the impulsive phase in most flares

TABLE 1
SPATIALLY UNRESOLVED CHARACTERISTICS OF THE FLARES

Event Number	Date	Time, HXR Peak	Time, Reference	GOES Class	t_{decay} (minutes)	T (Fe xxv) (10^6 K)	EM (Fe xxv) (10^{48} cm^{-3})	Ratio in L	Ratio in M1
1	1991 Dec 15	14:21:45	14:22:28	M1.0	1.5	21.6	2.7	0.41	0.13
2	1991 Dec 18	10:27:42	10:28:46	M3.6	2.5	22.0	10.5	0.61	0.31
3	1991 Dec 26	07:28:22	07:28:49	M2.9	1.0	20.2	0.71	0.12	<0.01
4	1991 Dec 26	21:36:57	21:38:18	M4.2	11.9	22.0	6.59	0.35	0.05
5	1991 Dec 27	< 06:10	06:12:40	M2.1	>5.8	21.2	5.77	0.54	0.17
6	1991 Dec 28	12:26:19	12:27:40	M3.3	2.5	21.0	13.4	0.67	0.20
7	1992 Jan 13	17:28:10	17:29:35	M2.0	5.7	22.6	5.14	0.88	0.25
8	1992 Jan 30	02:28:53	02:31:19	M1.6	6.6	19.6	4.91	0.66	0.29
9	1992 Feb 4	03:57:38	04:00:36	M1.6	3.7	18.9	4.25	0.44	0.18
10	1992 Feb 6	20:52:50	20:57:05	M4.1	8.2	20.7	10.0	0.50	0.16
11	1992 Feb 7	11:54:28	11:56:35	M3.7	4.7	19.7	10.8	0.92	0.20
12	1992 Feb 17	15:42:07	15:43:29	M1.9	5.4	18.3	7.85	0.73	0.19
13	1992 Feb 19	03:48:24	03:53:05	M3.7	6.4	18.7	15.1	0.66	0.29
14	1992 Feb 19	14:46:59	14:51:05	C8.0	8.5	21.4	1.02	0.36	0.08
15	1992 Mar 15	< 01:51	01:52:22	M7.8	>25	19.3	9.9	1.10	0.41
16	1992 Jun 25	17:54:25	17:57:53	M1.4	4.2	19.3	5.32	0.51	0.14
17	1992 Jul 3	09:48:09	09:51:58	M2.1	6.1	20.8	5.85	0.37	0.10
18	1992 Jul 18	< 13:42	13:44:59	M2.0	>4.2	20.8	4.47	1.07	0.74
19	1992 Aug 11	22:25:20	22:26:33	M1.4	4.4	20.2	7.21	0.37	0.08
20	1992 Aug 21	11:03:10	11:05:17	M1.0	6.1	21.0	3.66	0.97	0.65
21	1992 Sep 5	11:27:16	11:29:28	M4.0	1.9	22.4	7.05	0.61	0.30
22	1992 Sep 6	05:15:22	05:15:56	M2.4	2.9	21.2	7.23	0.69	0.15
23	1992 Sep 6	09:03:31	09:07:14	M3.3	3.9	19.5	8.00	0.72	0.41
24	1992 Sep 7	08:52:46	08:56:22	M1.2	5.8	19.9	3.21	0.58	0.23
25	1992 Sep 9	02:10:31	02:13:30	M3.0	6.4	20.5	8.54	0.98	0.51
26	1992 Sep 10	22:52:26	22:56:31	M3.2	5.2	20.9	8.54	0.79	0.26
27	1992 Sep 11	02:59:47	03:00:33	M1.1	2.6	18.6	3.14	0.69	0.27
28	1992 Oct 5	09:24:58	09:29:08	M1.8	7.0	20.5	5.14	0.99	0.53
29	1992 Oct 19	17:54:46	17:55:58	M1.1	>3.3	19.7	2.58	0.54	0.25
30	1992 Oct 27	01:45:28	01:47:01	M1.5	4.1	20.1	3.11	0.37	0.12
31	1992 Nov 5	06:19:24	06:20:21	M2.0	3.1	19.9	7.23	0.49	0.05
32	1993 Feb 11	18:31:40	18:32:55	M2.7	2.5	21.4	5.68	0.76	0.34
33	1993 Jun 7	14:21:16	14:22:18	M5.4	>3.5	...[a]	...	...	...
34	1993 Sep 27	12:08:33	12:11:47	M1.8	7.3	21.8	4.74	0.89	0.20
35	1993 Oct 9	08:08:24	08:11:07	M1.1	4.7	19.8	3.58	0.90	0.49
36	1993 Dec 25	17:54:40	17:55:19	M1.5	2.0	23.3	4.15	0.41	0.19

[a] BCS data saturated.

(see Fig. 1). It is this interval at which we characterize the flare in various ways described below. The *GOES* X-ray class is shown in the fifth column. All the flares belong to the *GOES* M class (e.g., M3.6 means a peak 1–8 Å flux of 3.6×10^{-5} W m^{-2}, as measured by the *GOES* satellite, preflare background not subtracted), with the exception of a C8.0 event (No. 14), i.e., one having a peak 1–8 Å flux of 8.0×10^{-6} W m^{-2}. The sixth column shows the hard X-ray decay time, defined by the HXT L channel at 10% of the peak. The inequality sign on this entry means that the spacecraft entered night before the flare decayed to the 10% level. Except for events 15, 18, and 33, our flares did not last long enough to be classified as long decay events.

3.2. *Comparison between BCS and HXT*

We derive temperature and emission measure at interval B (represented by the reference time in the fourth column of Table 1), applying the standard fitting technique on the Fe xxv spectrum obtained by the *Yohkoh* Bragg Crystal Spectrometer (BCS; Culhane et al. 1991). By this interval, the blueshifted asymmetry of the spectral lines, which is almost invariably seen early in disk flares and interpreted as a signature of chromospheric evaporation, has already subsided to a negligible level, so the fitting assumes a single

(stationary) component. The results are given in the seventh and eighth columns of Table 1. The values are somewhat different from those given by Jakimiec et al. (1998), partly because the intervals are different. The fitted temperatures are in the range of 18–23.5 MK. We then fold these emission-line temperatures and emission measures into the HXT response and obtain predicted count rates for the L and M1 channels. The last two columns of Table 1 shows the ratio of the expected count rate with that actually observed for the L and M1 channels, respectively. Except for events 15 and 18, which had already been well into decay when *Yohkoh* started observing them, the ratio for the L channel is smaller than unity. The ratio is much smaller for the M1 channel. Therefore, the BCS temperature and emission measure obtained with the isothermal assumption do not fully explain the HXT count rate, especially in the M1 channel. We interpret the two cases of L ratio exceeding unity as evidence for small calibration errors in one or the other of the two instruments or in the fitting procedures.

3.3. *Morphological Evolution*

The spatially resolved characteristics of the flares are given in Table 2. The third column shows the angular distance of the flare in Cartesian coordinates from disk center

TABLE 2
SPATIAL CHARACTERISTICS OF THE FLARES

Event Number	Date	Location $(x, y)/r_\odot$	FP to LT Evolution	L-Channel and SXR Loops	L-Channel to SXR Offset (SXT pixels [2″.46])[b]	Position of M1[c]	SXR Motion (SXT pixels [2″.46] per 5 minutes)[d]	High-T Region[e]
1	1991 Dec 15	(0.66, 0.12)	Yes	Same	(0.27, −0.36)	A	(0.18, −0.06)	D
2	1991 Dec 18	(−0.99, −0.24)[a]	No	Separate	(−2.33, 0.85)	A	(−0.27, 0.01)	D
3	1991 Dec 26	(0.21, −0.18)	Yes	Same	(−0.05, −0.07)	A	...	D
4	1991 Dec 26	(−0.31, 0.22)	No	Separate	(5.65, 0.66)	B	(−0.39, 0.55)	D
5	1991 Dec 27	(−0.54, −0.28)	No	Separate	(−1.63, 0.04)	C	(−0.21, −0.27)	A
6	1991 Dec 28	(0.60, −0.26)	No	Same	(−0.11, −1.28)	A	...	D
7	1992 Jan 13	(0.99, −0.27)	Yes	Same	(1.53, 0.24)	C	(0.17, −0.01)	B
8	1992 Jan 30	(0.04, 0.07)	No	Same	(1.74, 0.33)	E	(0.23, 0.13)	B
9	1992 Feb 4	(0.86, 0.17)	No	Separate	(2.76, −0.40)	E	(0.30, −0.19)	D
10	1992 Feb 6	(1.03, 0.11)[a]	No	Same	(2.44, 0.11)	C	(0.19, −0.01)	D
11	1992 Feb 7	(0.77, −0.21)	No	Both	(−0.82, −1.21)	C	(0.24, −0.07)	D
12	1992 Feb 17	(0.97, 0.30)	Yes	Same	(−0.40, 0.53)	E	...	D
13	1992 Feb 19	(−1.00, 0.08)	No	Both	(−1.81, −0.55)	C	...	B
14	1992 Feb 19	(−1.00, 0.10)[a]	No	Same	(−0.78, 0.47)	C	...	D
15	1992 Mar 15	(−0.48, −0.20)	...	Separate	(−2.19, 2.68)	D	(−0.04, 0.17)	D
16	1992 Jun 25	(0.98, 0.17)	No	Separate	(3.93, −3.23)	E	(0.25, −0.35)	B
17	1992 Jul 3	(−0.45, 0.15)	No	Separate	(10.31, 0.53)	D	(1.74, −0.11)	A
18	1992 Jul 18	(1.01, −0.20)[a]	...	Same	(0.35, −0.47)	E	...	D
19	1992 Aug 11	(−0.97, 0.24)	No	Both	(−1.56, −0.40)	B	(−0.37, 0.12)	D
20	1992 Aug 21	(0.67, 0.19)	No	Separate	(17.12, −1.29)	D	(0.40, 0.21)	A
21	1992 Sep 5	(0.40, −0.26)	Yes	Same	(−0.67, −0.74)	A	(0.22, 0.05)	D
22	1992 Sep 6	(0.63, −0.25)	Yes	Same	(1.45, −1.46)	C	(0.50, −0.26)	B
23	1992 Sep 6	(0.56, −0.25)	No	Same	(1.00, 1.33)	A	(0.25, 0.24)	D
24	1992 Sep 7	(0.78, −0.25)	No	Same	(−1.08, −1.65)	E	(−0.09, −0.19)	A
25	1992 Sep 9	(0.98, −0.18)	No	Same	(2.11, 1.03)	C	(0.33, 0.07)	D
26	1992 Sep 10	(−0.64, 0.21)	Yes	Same	(−1.61, −0.85)	C	(−0.12, −0.17)	B
27	1992 Sep 11	(−0.62, 0.20)	No	Same	(0.75, 0.30)	E	(0.01, 0.59)	D
28	1992 Oct 5	(1.03, −0.14)[a]	No	Same	(1.76, 0.38)	E	(0.17, 0.02)	D
29	1992 Oct 19	(−0.40, 0.02)	No	Separate	(8.50, 1.28)	E	(0.14, 0.52)	A
30	1992 Oct 27	(0.28, 0.48)	Yes	Same	(−0.97, 0.65)	A	...	D
31	1992 Nov 5	(0.98, −0.31)[a]	No	Same	(−0.32, −0.82)	B	(0.08, −0.29)	D
32	1993 Feb 11	(0.30, 0.05)	No	Same	(0.17, 0.22)	E	...	D
33	1993 Jun 7	(0.50, −0.17)	No	Same	(0.87, −0.65)	B	(0.34, −0.01)	C
34	1993 Sep 27	(−0.99, 0.16)	Yes	Same	(−1.15, 0.18)	B	(−0.24, 0.26)	B
35	1993 Oct 9	(1.00, 0.17)	No	Same	(−0.03, 0.75)	E	(0.11, 0.57)	D
36	1993 Dec 25	(−0.10, 0.18)	No	Same	(−0.10, 0.59)	A	(−0.22, −0.05)	C

[a] Footpoints occulted (Jakimiec et al. 1998).
[b] Note that the uncertainty is ∼0.5 pixels, reflecting the co-alignment accuracy.
[c] A: Same as L. B: Lower than L. C: Higher than L. D: Poor image quality, presumably because of the extended source. E: No M1 image available because of insufficient counts.
[d] Note that the uncertainty is 0.1–0.3 pixels, depending on the constancy of the motion over the time of measurement.
[e] A: Overlap with L. B: Above L. C: Displaced from L, but the height relation is not known. D: Nonexistent.

as a vector normalized to the solar radius, so that one can readily see the radial direction. We note that 14 flares occurred at the limb. We study the time evolution of the flares from the earliest to the last HXT and SXT data available to see if the morphology mimics what is expected from the scenario based on chromospheric evaporation, i.e., transition of the dominant emission from double footpoints to loop-top (see Figs. 2 and 3). This is summarized in the fourth column of Table 2, where LT and FP stand for loop top and footpoints, respectively. We note that flares clearly showing this transition are a minority (eight of 36). Not many flares show double-footpoint sources even in the highest-energy channel that has enough counting statistics for image reconstruction. One obvious reason for this is that the footpoints may be occulted by the limb. Jakimiec et al. (1998) indicated six flares in this category. Other possible reasons for the absence of double-footpoint sources would include strong loop emission even in the early phase (see

Sato 2000), unresolved footpoints, large loop asymmetry, or complicated geometry not describable as a simple loop. If the two footpoints are not clearly defined, it is not easy to locate the loop top, but in these flares we assume the single bright source following the impulsive phase to be the loop-top source.

3.4. Relation between SXR and HXR Sources

The co-aligned SXT and HXT images reveal that low-energy HXR emission in the gradual phase sometimes comes predominantly from an extended structure separate from the SXR loop. One example is the flare shown in Figure 4, and another was given by Nitta & Yaji (1997), which is also included in this study as event 20. This is found to be the case for a quarter (nine of 36) of the flares, which are labeled "separate" in the fifth column of Table 2. In three flares, the hard X-ray sources come both from the soft X-ray loop and from a separate structure. These are

labeled "both." For the flare in Figure 4, images with twice the field of view (Fig. 5) indicate that the extended structure corresponds to a loop system connecting the preceding spot (not included in Fig. 4) and the following spot in an active region. The footpoints of this loop system are separated by $\gtrsim 5 \times 10^4$ km.

In the remaining 24 flares in this study, the HXT L-channel source is compact and located close to the SXT source, suggesting that it belongs to the same bipolar structure. But even in these flares, the two sources are rarely cospatial. The sixth column of Table 2 shows the offset of the HXT L-channel source from its counterpart in the SXT Be image, expressed in SXT full-resolution pixels ($2''.46$). The centroid of either source is calculated using the pixels above 30% of the peak. In more than half of these flares (14 of 24), as in those in which a structure separate from the soft X-ray loop contributes to the hard X-ray emission, we find that the offset exceeds 1 SXT pixel, well above the estimated co-alignment errors (Masuda 1994). For flares at or near the limb, the HXT L-channel source is usually displaced toward higher altitudes (see Fig. 3), with the exception of event 31. However, for some disk flares, the displacement is far from the radial direction. For these flares, the directions of the offsets are also displayed in Figure 6, which also indicates the limb and disk center.

In the seventh column of Table 2, we indicate the location of the M1-channel source with respect to the L-channel source. First, 11 of the 36 flares did not have enough counts in the HXT higher-energy channels in interval B for image synthesis (category E). For the remainder of the flares, apart from the three that had poor image quality (category D) due presumably to the extended nature of the source (see Fig. 4), the M1-channel source appears to be cospatial with (category A, eight of the 22 remaining flares), lower than (category B, five of the 22 flares), or higher than (category C, nine of the 22 flares) the L-channel source. We believe that Category B reflects residual emission from low altitudes (near footpoints) that characterizes the impulsive phase.

3.5. *Motion of the SXR Source*

According to reconnection models in simple bipolar configurations (see, e.g., Forbes & Acton 1996; Yokoyama & Shibata 1997; Somov, Kosugi, & Sakao 1998), successively higher field lines reconnect to form closed loops as the flare progresses. The SXR loop-top source, which represents evaporated plasma in those loops, would therefore appear
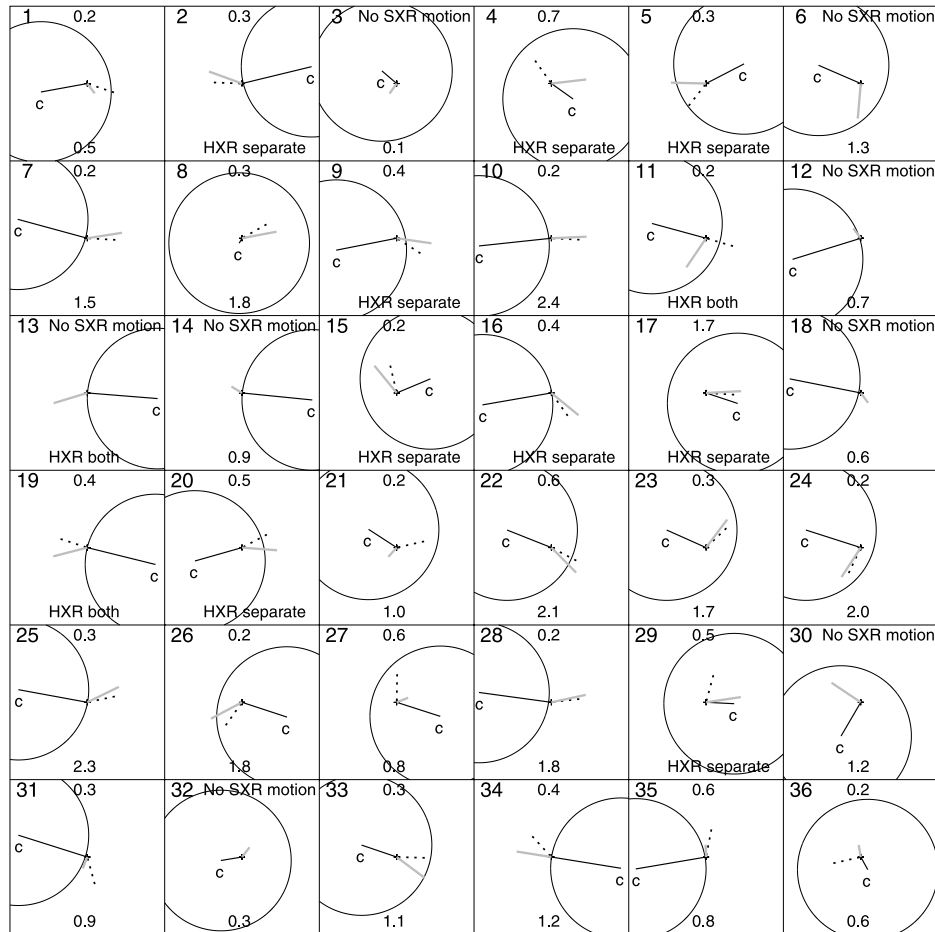

FIG. 6.—For each of the 36 flares: (1) the location of the flare (brought to the center) with respect to disk center (*marked* "c") and the limb, (2) the direction of the offset of the HXT L-channel source from the soft X-ray loop-top source (*gray lines*; see § 3.4), and (3) the direction in which the soft X-ray loop-top source seems to move in the gradual phase (*dotted lines*; see § 3.5). Amplitudes in SXT pixels for data points 2 and 3 are given by the lower and upper numbers, respectively. For data point 2, longer lines are used for the flares in which the offset of the HXT L-channel source exceeds 1 SXT pixel. No information is given for flares in which the HXT L-channel sources include a separate and extended structure. We use the label "No SXR motion" when the motion of the soft X-ray source is less than 0.20 pixels per 5 m.

to rise with time. In order to find out if the data are consistent with this prediction, we trace the motion of the SXR source with time, calculating the position of the centroid of the pixels that are above 30% of the peak. The calculated motion is given in the eighth column of Table 2. The unit is SXT full-resolution pixels per 5 minutes, or 6 km s^{-1} if thought of as a velocity. The results are also displayed in Figure 6, which shows the direction of the motion for each event. The measurement has large uncertainties, especially because the apparent motion often changes direction during the flare. Most (10 of 14) limb flares show motions consistent with rising, although the direction is sometimes far from radial (four flares). Disk flares show a variety of directions, similar to the HXR-SXR offset, possibly reflecting the complicated geometry involving tilts (inclinations) and asymmetries of the loops (Nitta, van Driel-Gesztelyi, & Harra-Murnion 1999). We note that the motion of the SXR loop-top source, even in limb flares, is much slower than that of the plasmoid-like ejecta, which are considered by some (see, e.g., Shibata et al. 1995) to trigger fast reconnection. The tendency for the loop-top source to be nearly stationary may present a difficulty for interpretation in terms of standard reconnection models in simple bipolar configurations.

3.6. Relation between the SXT High-Temperature Region and the HXT L-Channel Source

The bottom panels of Figures 2–4 present SXT temperature maps obtained from the ratio of a pair of images in thick Al and Be filters. In SXT temperature maps of flares, we frequently see high-temperature pixels away from the bright pixels; in other words, the brighter regions typically have lower filter-ratio temperatures. Some authors have attached special meaning to these high-temperature pixels (see, e.g., Masuda et al. 1994), especially in connection with reconnection theories, which might predict the presence of superhot regions above the SXR loop. However, these high-temperature pixels can be questionable because of several factors, among which the point-spread function (including scattering from the grazing-incidence mirror) may be the most important. Caveats for SXT temperature maps of flares are discussed in the Appendix. Unfortunately, judgment as to the reality of the high-temperature pixels has not previously been made in a fully objective manner. Often-used criteria for the reality of the high-temperature pixels (see, e.g., Doschek 1999) include (1) their distribution may be wider than 1–2 pixels, (2) they appear consistently from one temperature map to the next, (3) they occur where the intensity is not extremely low, and (4) they do not show strong dependence on changes in image intensity. Each of these signatures could equally well come from systematic errors. We feel that it is premature to draw strong conclusions from subtle effects in flare temperature maps.

Using the above criteria, however, we find in any case that high-temperature pixels of solar origin are absent in 22 flares (category D in the ninth column of Table 2). Among the remaining flares, where the high-temperature pixels *may be* of solar origin, the typical (seven of 14 flares) pattern is that they are located above the HXT L-channel source (category B in Table 2; see Fig. 3). Even for those flares where the high-temperature pixels at first sight seem to have good overlap with the L-channel source (category A, five of 14 flares), they are not strictly cospatial. A close look at Figure 4 reveals significant displacements between the L

counts (*dotted lines*) and the SXT temperatures in all three epochs. In two events there is no clear way to explain the offset of the two sources in terms of a difference in heights, because they are located at nearly the same distance from the disk center.

3.7. Comments on TRACE Observations in Fe xxiv

Recently, Warren et al. (1999) have presented an analysis of high-resolution data from the *Transition Region and Coronal Explorer* (*TRACE*; Handy et al. 1999), predominantly showing the Fe xxiv line in the 195 Å channel, and have compared them with SXT images and temperature maps. The flare, a large two-ribbon event that occurred on 1999 July 25, showed a fringe of hot pixels resembling those in Figures 2 and 3. Warren et al. were able to show that the SXT filter-ratio temperature and emission measure in the hot-pixel region successfully predicted the *TRACE* response in Fe xxiv. Although this may appear to undermine the importance of the systematic errors in SXT temperature maps we discuss in the Appendix, we have to recall that the SXT filter-ratio temperatures must reflect the presence of any multithermal plasma in the line of sight. Therefore the *TRACE* Fe xxiv response, essentially at one temperature, cannot unambiguously show how serious the SXT systematic errors may be in a single event.

4. TEMPERATURE DISTRIBUTION

In this section we assess what can be concluded about the distribution of plasma with different temperatures in the flare, including the loop top, by using the SXT, BCS, and HXT measurements. We first emphasize that none of the instruments can extract the plasma temperature at a given position in a flare. SXT and HXT are broadband instruments, and their filter-ratio or channel-ratio temperatures are merely convolutions of the differential emission measure and instrument sensitivity with respect to temperature. In principle, BCS provides a better diagnostic for plasma temperatures. We also know that the emission for the Fe xxv and Ca xix channels must come from the flare. However, it is not possible to obtain the spatial distribution of plasma *within* the flare.

Here we try a better use of SXT flare-sequence data, which usually include full-resolution images in three filters, Be, thick Al, and thin Al. Most quantitative studies of flares based on SXT data in the past have taken the temperature at face value from the ratio of the two thickest filters (Be and thick Al), assuming that every pixel is occupied by plasma of a single temperature. Typical flare temperatures obtained in this way are in the 10–20 MK range. Nitta & Yaji (1997) first pointed out the inadequacy of such analyses, by demonstrating that the temperatures and emission measures from the Be-thick Al ratio, convolved with the BCS response, give a significantly lower temperature than the one actually obtained from the Fe xxv-channel data. The discrepancy between the expected and observed BCS temperatures is attributable to the presence of cool plasma in the line of sight not detected by BCS. Such cool plasma also makes the Be/thin Al temperature (denoted by T_1) lower than the Be/thick Al temperature (denoted by T_2).

As the simplest step beyond the isothermal assumption, we consider a two-temperature model characterized by two sets of temperatures and emission measures (T_L, EM_L and T_H, EM_H), with $T_L \leq T_H$. From images in three filters, we cannot obtain all four parameters. But if we fix one param-

eter, the other three are uniquely determined. Here we fix T_H to 20, 30, and 40 MK and study the relation of the parameters T_L and EM_H (normalized to EM_2, which is associated with T_2) with the assumed observed temperatures T_1 and T_2 (Fig. 7). We can easily adjust the intensity in the three filters to reproduce a given set of T_1 and T_2. Note that $T_L \leq T_1 \leq T_2 \leq T_H$. We consider three representative cases of T_2: 19, 16, and 11 MK. In Figure 7, different symbols represent different values of T_2. Adjacent symbols on each line represent 0.5 MK differences in T_1, starting from $T_1 = T_2 - 0.5$ MK at the rightmost point. For a given T_H, we note that the difference between T_1 and T_2 becomes larger for a lower T_L. Moreover, plasma of T_H (much hotter than T_2) could be present as long as $T_2 > T_1$, with EM_H not much smaller than EM_2. For example, according to the rightmost plot, plasma of 40 MK can exist even when $T_2 = 16$ MK, and its emission measure EM_H is as much as 59% of EM_2 if $T_L = 9$ MK.

Although the two-temperature approach is certainly an oversimplification, it is still much more realistic than taking a filter-ratio temperature, such as T_2, at face value. Using the measured values of T_1 and T_2 (or equivalently the number of electrons per second in thin Al, thick Al, and Be filters), we now try to find out how localized the ~ 20 MK plasma should be. We assume T_H to be the same as the BCS Fe xxv temperature (shown in Table 1) everywhere in the SXT image, and we obtain and sum the contributions to EM_H, starting from the brightest pixel in the Be image, until the sum equals the BCS emission measure. In all the flares that seem to produce reasonable temperature maps, we find that at least the whole loop must be summed to explain the BCS EM, as given in Table 1. For the 1992 January 13 flare (Fig. 3), for example, we need the 90 brightest pixels, which nearly covers the entire loop. The SXT filter-ratio temperature for the loop is heavily affected by cooler plasma in the same line of sight. In other words, the SXT high-temperature pixels alone do not provide enough EM to be consistent with the BCS observations, even though their filter-ratio temperature is sometimes close to the BCS Fe xxv temperature (Doschek 1999).

Based on the two-temperature model, we can also get an improved estimate of the temperature of the SXT high-temperature region, which is often located above the HXT L-channel source. Figure 7 shows that the emission measure of the hot component (EM_H) is a significant fraction of the emission measure from the Be-thick Al filter ratio (EM_2). Therefore, for a higher T_H, the expected HXT counts can exceed the observed counts. Indeed, for the 1992 January 13

flare, we should have $T_H \lesssim 20$ MK for the SXT high-temperature region, so that it does not contribute to the HXT counts. Therefore, to satisfy all the SXT, HXT, and BCS observations, the region where the SXT filter-ratio temperature is the highest (above the loop top) does not seem to be particularly hot, as compared with the loop, which we assume is filled with ~ 22.6 MK plasma to account for the BCS observations.

We now derive the physical parameters for the loop-top source seen in the HXT L-channel images. For the 1992 January 13 flare, the ratio of the L and M1 channels yields $T = 31.5$ MK and $EM = 3.9 \times 10^{47}$ cm^{-3} over 43 pixels, resulting in $EM = 9.1 \times 10^{45}$ cm^{-3} pixel^{-1}. If we subtract out the contributions from the ~ 20 MK plasma that are more pronounced in the L channel than in the M1 channel, the HXR loop-top source has $T = 45.3$ MK and $EM = 5.6 \times 10^{44}$ cm^{-3} pixel^{-1}. Because of the small emission measure, this superhot plasma hardly affects the SXT temperature measurements. Moreover, the emission measure may be too small for the BCS Fe xxvi diagnostic to produce appropriate temperature information. In summary, combination of SXT, HXT, and BCS data implies the highest temperature of the plasma to be $\gtrsim 20$ MK, ~ 45 MK, and $\lesssim 20$ MK, respectively, in, slightly above, and farther above the soft X-ray loop.

Without better imaging spectroscopy having continuous coverage in energies, we may not be able to rule out completely the possibility that the M1-channel source and some part of the L-channel source in fact represent nonthermal electrons trapped in the corona, as suggested by Metcalf & Alexander (1999) for the hard X-ray sources during the impulsive phase. However, this explanation may not be likely for the hard X-ray sources in the gradual phase. The observed M1-L ratio in the gradual phase corresponds to a steep power-law spectrum (the power-law index of -6.7 for the 1992 January 13 flare), and such a spectrum would produce many more signals in SXT images than observed, unless an artificial low-energy cutoff of the trapped electrons is set to be quite high, e.g., >30 keV. This requires an artificial high-energy cutoff to be set at a quite low value (<50 keV) to keep the M1-L ratio unchanged. But such a high-energy cutoff, in turn, is inconsistent with the finite photon flux in the M2 channel, as seen in many flares, including the 1992 January 13 flare.

5. DISCUSSION AND CONCLUSIONS

In this paper, we study the 36 flares analyzed by Jakimiec et al. (1998). Except for the noticeable Fe xxvi emission in
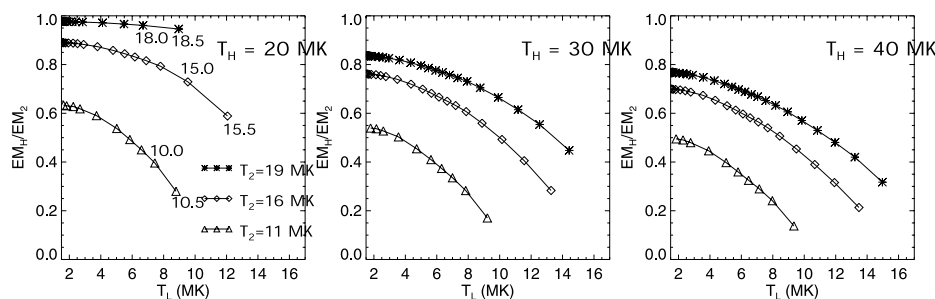

FIG. 7.—How representative Be/thick Al filter-ratio temperatures ($T_2 = 19$, 16, and 11 MK) can result from two-temperature (T_H and T_L) plasma with corresponding emission measures (EM_H and EM_L) when the Be/thin Al temperature T_1 is lower than T_2. T_H is fixed, and the three plots correspond to given values of T_H: 20 MK (left), 30 MK (middle), and 40 MK (right). For each value of T_2, T_1 is assumed to be $T_2 - 0.5i$ ($i = 1, 2, \ldots$). The mapping between (T_1, T_2) and (T_L, EM_H) is shown.

the *Yohkoh*/BCS measurement (Pike et al. 1996), these flares are probably representative of all flares with similar soft X-ray peak fluxes (i.e., M-class according to the *GOES* 1–8 Å measurement). In conducting our analysis, we try to compare the results with possible outcomes of a currently popular scenario. This assumes a black-box energy release region (due to magnetic reconnection) above the bright loop seen in soft X-rays. The loop is considered to be filled with hot plasma ablated from the loop footpoints in response to the bombardment of nonthermal electrons produced at the energy release site. The hot plasma is confined at the loop top. In order for reconnection to proceed, field lines at successively higher altitudes have to be reconnected to form closed loops. As a result, we expect the loop-top source to rise with time. The reconnection models may also predict the presence of a very hot region at the energy release site, or between the energy release site and the loop top (see, e.g., Forbes & Acton 1996).

As expected, we see a wide variety of morphologies among different flares. However, the HXT L-channel source, which we consider to represent superhot plasma, is consistently (13 of 14 flares) located above the soft X-ray loop, as far as limb flares are concerned (see Fig. 6). This includes flares in which the L-channel source comes from a separate structure or the offset of the L-channel source is less than 1 SXT pixel. The L-channel source for the remaining limb flare (event 31) may be affected by emission from low altitudes in an occulted loop; in this flare, the M1-channel source appears to be lower than the L-channel source. Concerning the motion of the soft X-ray loop-top source, the direction is again roughly consistent with the direction of increasing height for limb flares. However, the speed is very low ($\lesssim 10$ km s^{-1}) in comparison with the typical speed (50–400 km s^{-1}) of the hot plasma ejections suspected of inducing reconnection (Shibata et al. 1995).

In the gradual phase of flares, the ~ 20 MK plasma contributes significantly to the HXT L channel and somewhat to the M1 channel. With these contributions subtracted, the M1-L ratio yields a superhot temperature, which is also consistent with a steep ($\gamma \gtrsim 6$) power-law spectrum. As discussed in § 4, we believe that this is more consistent with superhot plasma than with trapped electrons, which would produce much larger signals in SXT images than observed. An artificial low-energy cutoff of the nonthermal electrons does not help, because it leads to a low high-energy cutoff (to maintain the observed M1-L ratio), which may cause the M2 count to be smaller than observed. Therefore, apart from the theoretical difficulty of keeping the superhot plasma from rapidly disappearing because of thermal conduction, the HXT sources must come from the superhot plasma. As another important point, the emission measure of the HXT source (per pixel) is so low that it does not affect SXT filter-ratio temperatures. That is, the HXT L and M1 channels are more sensitive than SXT to superhot plasma.

The M1-channel source is often seen to be located slightly higher than the L-channel source. This may indicate a small temperature gradient with increasing height, while the opposite case may represent contributions of emission from low altitudes that was strong in the impulsive phase. Without such contributions, the M1-channel source may always be slightly higher, and the cospatial L-channel and M1-channel sources in some flares may result from a combination of geometrical factors (the tilt, inclination, and asymmetry of the loop) and the measurement accuracy. In addition to these HXT sources, we sometimes see a high-temperature region in SXT temperature maps, but it cannot represent superhot plasma; otherwise it should be bright in HXT. Based on limb flares (events 7, 13, and 34), such a region seems to be located higher than the HXT sources. Summarizing these observations, the temperature may peak not far above the soft X-ray loop. This probably corresponds to an energy release region also located close to the loop. The slow rising motion of the soft X-ray loop-top source suggests that the energy release region rises only slightly, possibly bound by overlying structures. Incidentally, in 21 flares we note plasma ejections of the type reported by Shibata et al. (1995). For limb flares, we cannot trace the ejection over a certain height ($\sim 1.2 \, R_\odot$).

In conclusion, we have found observational complexities not discussed by Jakimiec et al. (1998), because we pay attention to more details of the data. Those flares in which the superhot plasma comes from a structure separate from the main flare loop do not seem to conform to the model proposed by Jakimiec et al. (1998), nor are they explained in terms of reconnection models in a simple bipolar configuration. Observations of this type of flare on the disk remind us that reconnection is a three-dimensional process. The standard two-dimensional reconnection models are consistent with some observational results (such as the superhot plasma above the soft X-ray loop), but multiple bipoles appear to be involved in some flares. The slight offset of the low-energy hard X-ray source from the soft X-ray loop-top source may also be attributable to the superhot plasma, again not mentioned by Jakimiec et al. (1998). A complete picture of the plasma distribution at different temperatures may be available only with a better imaging spectroscopy, such as the one we anticipate to be available with the *High-Energy Solar Spectroscopic Imager* (*HESSI*) mission. In addition, we would like to confirm the presence of the superhot plasma in the Fe xxvi channel of *Yohkoh*/BCS and to encourage improvements in calibration and data analysis software.

APPENDIX A

EVALUATION OF SXT TEMPERATURE MAPS FOR FLARES

In order to determine the reality of the high-temperature pixels seen in SXT filter-ratio temperature maps for flares, we should understand possible causes of systematic errors. Tsuneta et al. (1991) presented full background information for this discussion. Systematic errors can degrade SXT temperature maps in combination, and a single cause may not be easily identified. Here we briefly discuss (1) statistical errors, (2) the inadequate characterization of the SXT point-spread function
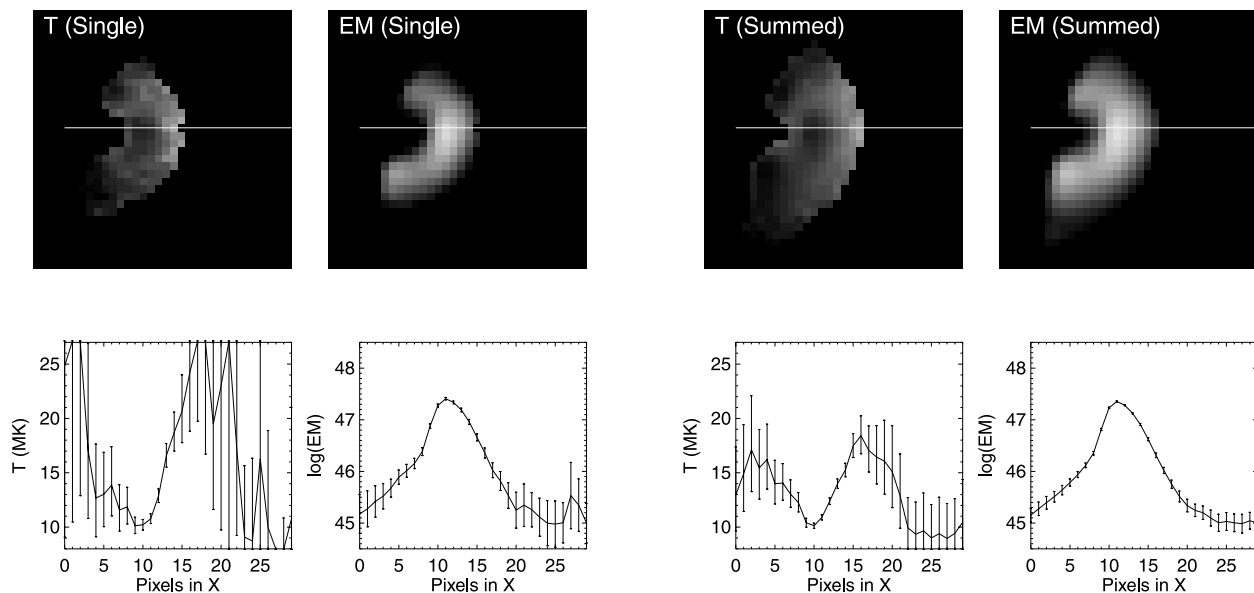
FIG. 8.—Comparison of the noise level of the SXT filter-ratio temperature and emission measure for a pair of snapshots (*left*) and a pair of summed images composed of six snapshots (*right*). Images used in the left panel were taken at 17:29:35 (Be) and 17:29:39 (thick Al) on 1992 13 January. Those used in the right panel were taken between 17:28:05 and 17:31:03. The exposure duration of the single Be image is 58 ms, but that of the summed Be image is 530 ms.

(PSF), and (3) the possibility of erroneous pointing information used to correct for spacecraft jitter. Other causes may include errors involved in subpixel image registration (affecting pixels located where there is a large gradient in intensity) and the lack of full corrections of the SXT off-axis response (vignetting). The vignetting corrections are more important for flares closer to the limb. The vignetting correction is wavelength-dependent, but the standard software simply uses the prelaunch calibration data for 4.16 Å for images in both thick Al and Be. This certainly results in overcorrection, especially for the images in thick Al, because the effective wavelengths are $\gtrsim 8.5$ Å for the temperature ranges of interest. We believe that an empirical calibration of the vignetting from in-flight data will be possible.

A1. STATISTICS

Estimates of the error from counting statistics are easily available, using the standard analysis software. These estimates include the quantization error from primary data compression. The flare is a bright object, but the automatic exposure control makes the exposure short enough to avoid saturation, resulting in a small number of electrons counted in each image pixel, especially in faint regions. The fact that the exposures are short effectively amplifies the dark current correction, because for short exposures the fixed CCD readout noise dominates. Figure 8 compares the error bars of Be-thick Al filter-ratio temperature maps when we use a single-image pair (*left*) and those from a summed-image pair (*right*). The top and middle panels represent temperature and emission measure, respectively, and the bottom panels plot these quantities across the line indicated in the top and middle panels. We see large error bars in the temperature for a single image pair (no time integration), although the emission measure has relatively small uncertainties. For this reason, the temperature maps analyzed in this paper reflect summation of several (five to eight) images in each filter before taking the ratio. We note that image summation based on pixels selected by temperature is incorrect, because noise fluctuations will introduce a bias (Doschek 1999).

A2. POINT-SPREAD FUNCTION

In Figure 8, we also note an increase in temperature toward the right, i.e., the corona, but also toward the left, i.e., toward lower altitudes. A stronger pattern is seen in the temperature maps presented in Figure 2. This temperature gradient toward apparent low altitudes likely comes from our incomplete understanding of the SXT point-spread function (PSF). The PSF consists of the sharply peaked core and the scattering wing. The core is well characterized by an elliptical Moffat function (Martens, Acton, & Lemen 1995), but there is an indication that it is wider at shorter wavelengths, a dependence possibly strong enough to produce an artificial high-temperature ring around a bright source in Be-thick Al filter-ratio temperature maps (see Jakimiec et al. 1998). Note that the mean wavelengths in Be and thick Al filters are, respectively, 5–6.5 Å and 8.5–10 Å, for temperatures between 10 and 30 MK.

However, we believe that the greatest source of misunderstanding of SXT temperature maps published to date is the contribution of scattering to the SXT PSF. Scattering due to the mirror microroughness certainly dominates the SXT images of the flaring Sun outside the flare's core regions. Using saturated flare images, Hara et al. (1994) characterized the scattering wing at a distance $\gtrsim 20''$ from the point source with a power law, but its connection to the core is still unclear (Shin 1998), and its possible strong wavelength dependence has hardly been explored. A serious work is under way (S. Akiyama, H. Hara, & T. Kosugi 2000, private communication) to assess and remove scattering from the SXT flare images. Until we have an adequate understanding of the effects of the PSF, we cannot be completely sure about the temperatures of the coronal high-temperature
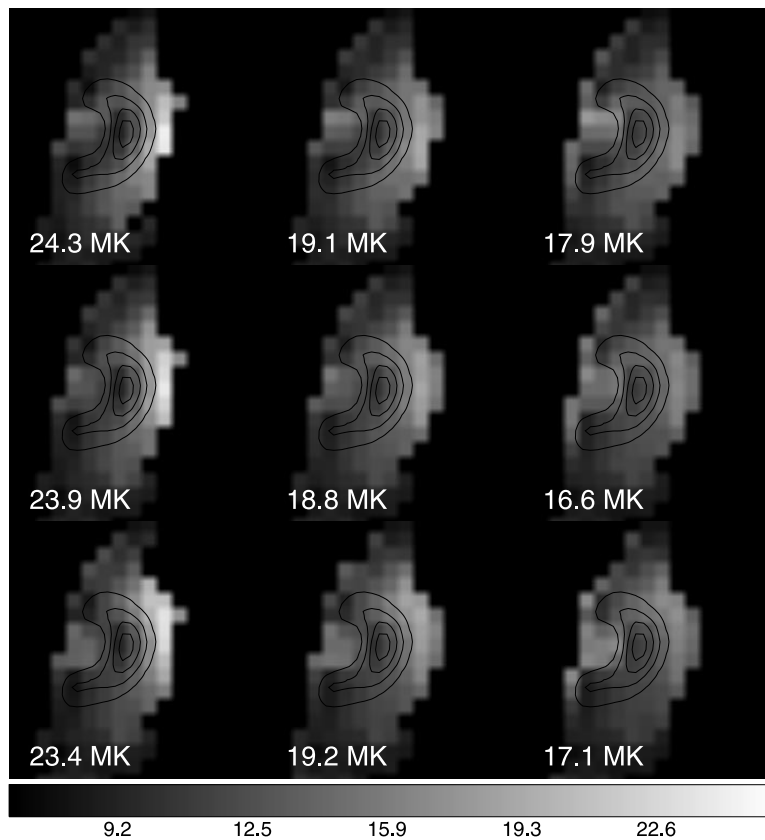
FIG. 9.—Effect of possible misalignment of the images. This shows SXT temperature maps for the 1992 January 13 flare, when the thick Al image is artificially shifted by 0.2 pixels in the corresponding directions—the central map has no shift. In each map, the maximum temperature is indicated and the intensity in Be filter is overplotted as contours. Note the large effects in the solar radial direction, which has the largest image gradients.

pixels (see Figs. 2 and 3). Subjective criteria, such as those listed in § 3.6, cannot easily distinguish true temperature variations from systematic errors.

A3. SPACECRAFT JITTER

Finally, we comment on the possibility that uncorrected spacecraft jitter may explain the spurious high-temperature edges in SXT temperature maps, as proposed by Siarkowski et al. (1996). Indeed, as shown in Figure 9, only a slight shift (0.2 pixels, or $0''.5$) of one member of the image pair can drastically change the appearance of the high-temperature regions, especially in the direction of the brightness gradients. The high-temperature region above the soft X-ray loop is enhanced in the maps in the left column, and almost vanishes in those in the right column. Siarkowski et al. (1996) actually suggested using this phenomenon to correct the pointing empirically, but this might systematically bias the resulting temperature map. As Siarkowski et al. pointed out, the spacecraft jitter resulting from filter-wheel motions may amount to several tenths of a pixel between successive exposures. Although such differences may appear large in the context of Figure 9, the standard analysis software adjusts for the displacements.
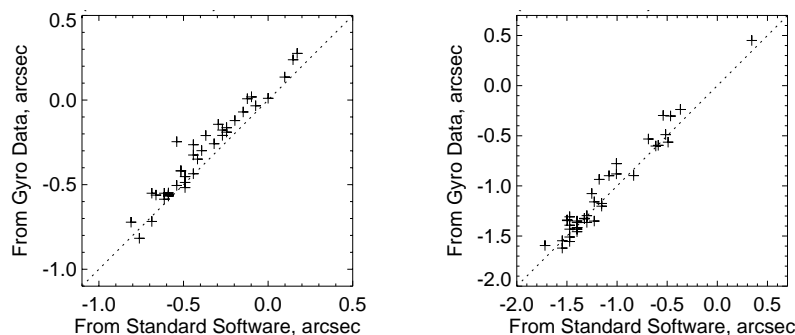

FIG. 10.—Magnitude of the scatter in the *Yohkoh* pointing corrections for images in Be and thick Al filters in the 1992 January 13 flare. For both axes of spacecraft motion, X in the left panel and Y in the right, the abscissae give the image displacements reported by the standard software, and the ordinates give the improved estimates based on better gyro sampling. The overall scale shows the range of jitter motions during the flare. Fig. 9 calibrates these displacements in terms of temperature errors.

We have reexamined the pointing corrections by making use of additional sampling of the *Yohkoh* gyros, the basic reference for spacecraft jitter motions. The standard software presently uses only one eighth of these samples. At the full-time resolution of the sampling, 0.25 s, we can study the possible effects of image latency (the time between the attitude data and the actual exposure) and image duration (a thick filter may require a long exposure even during flare conditions). The result of this can be seen in Figure 10, which compares the pointing offsets for the true time differences of the Be and thick Al images of the 1992 January 13 flare, as studied by Siarkowski et al. (1996). The scatter of the points indicates the scale over which a systematic error might be present and introduce a bias in an SXT temperature map, as shown in Figure 9. Future versions of the standard *Yohkoh* software will incorporate this improvement, whose importance will need to be assessed individually for each flare. At present we conclude that systematic errors due to pointing jitter are not as important as those due to scattering.

REFERENCES

Acton, L. W., et al. 1992, PASJ, 44, L71
Culhane, J. L., et al. 1991, Sol. Phys., 136, 89
Doschek, G. A. 1999, ApJ, 527, 426
Doschek, G. A., & Feldman, U. 1987, ApJ, 313, 883
Doschek, G. A., Strong, K. T., & Tsuneta, S. 1995, ApJ, 440, 370
Feldman, U., Hiei, E., Phillips, K. J. H., Brown, C. M., & Lang, J. 1994, ApJ, 421, 843
Forbes, T. G., & Acton, L. W. 1996, ApJ, 459, 330
Handy, B. N., et al. 1999, Sol. Phys., 187, 229
Hara, H., Tsuneta, S., Acton, L. W., Bruner, M. E., Lemen, J. R., & Ogawara, Y. 1994, PASJ, 46, 493
Hudson, H. S., & Nitta, N. 1996, in High Energy Solar Physics, ed. R. Ramaty, N. Mandzhavidze, & X.-M. Hua (New York: AIP), 285
Hudson, H. S., Strong, K. T., Dennis, B. R., Zarro, D., Inda, M., Kosugi, T., & Sakao, T. 1994, ApJ, 422, L25
Jakimiec, J., Tomczak, M., Falewicz, R., Phillips, K. J. H., & Fludra, A. 1998, A&A, 334, 1112
Kosugi, T., et al. 1991, Sol. Phys., 136, 17
Lin, R. P., Schwartz, R. A., Pelling, R. M., & Hurley, K. C. 1981, ApJ, 251, L109
Martens, P. C., Acton, L. W., & Lemen, J. R. 1995, Sol. Phys., 157, 141
Masuda, S. 1994, Ph.D. thesis, Univ. Tokyo
Masuda, S., Kosugi, T., Hara, H., Tsuneta, S., & Ogawara, Y. 1994, Nature, 371, 495
McTiernan, J. M., Kane, S. R., Loran, J. M., Lemen, J. R., Acton, L. W., Hara, H., Tsuneta, S., & Kosugi, T. 1993, ApJ, 416, L91

Metcalf, T. R., & Alexander, D. 1999, ApJ, 522, 1108
Nitta, N., van Driel-Gesztelyi, L., & Harra-Murnion, L. K. 1999, Sol. Phys., 189, 181
Nitta, N., & Yaji, K. 1997, ApJ, 484, 927
Ogawara, Y., Takano, T., Kato, T., Kosugi, T., Tsuneta, S., Watanabe, T., Kondo, I., & Uchida, Y. 1991, Sol. Phys., 136, 1
Pike, C. D., et al. 1996, ApJ, 464, 487
Sakao, T., Kosugi, T., & Masuda, S. 1998, in Observational Plasma Astrophysics: Five Years of *Yohkoh* and Beyond, ed. T. Watanabe, T. Kosugi, & A. C. Sterling, (Dordrecht: Kluwer), 273
Sato, J. 2000, ApJ, submitted
Sato, J., Kosugi, T., & Makishima, K. 1999, PASJ, 51, 127
Shibata, K., Masuda, S., Shimojo, M., Hara, H., Yokoyama, T., Tsuneta, S., Kosugi, T., & Ogawara, Y. 1995, ApJ, 451, L83
Shin, J. 1998, Ph.D. thesis, Graduate Univ. for Advanced Studies/Natl. Astron. Obs., Japan
Siarkowski, M., Sylwester, J., Jakimiec, J., & Tomczak, M. 1996, Acta Astron., 46, 15
Somov, B. V., Kosugi, T., & Sakao, T. 1998, ApJ, 497, 943
Tanaka, K. 1986, PASJ, 38, 225
Tsuneta, S., et al. 1991, Sol. Phys., 136, 37
Warren, H. P., Bookbinder, J. A., Forbes, T. G., Golub, L., Hudson, H. S., Reeves, K., & Warshall, A. 1999, ApJ, 527, L121
Yokoyama, T., & Shibata, K. 1997, ApJ, 474, L61